Experimental Demonstration of Efficient Spin–Orbit Torque Switching of an MTJ With Sub-100 ns Pulses

Tanay A. Gosavi[1], Sasikanth Manipatruni[2], Sriharsha V. Aradhya[1], Graham E. Rowlands[1], Dmitri Nikonov[2], Ian A. Young[2], and Sunil A. Bhave[3]

[1]Cornell University, Ithaca, NY 14850 USA
[2]Exploratory Integrated Circuits, Components Research, Intel Corp., Hillsboro, OR 97124 USA
[3]Purdue University, West Lafayette, IN 47907 USA

Efficient generation of spin currents from charge currents is of high importance for memory and logic applications of spintronics. In particular, generation of spin currents from charge currents in high spin–orbit coupling metals has the potential to provide a scalable solution for embedded memory. We demonstrate a net reduction in the critical charge current for spin torque-driven magnetization reversal via using spin–orbit mediated spin current generation. We scaled the dimensions of the spin–orbit electrode to 400 nm and the nanomagnet to 270 nm × 68 nm in a three-terminal spin–orbit torque, magnetic tunnel junction (SOT-MTJ) geometry. Our estimated effective spin Hall angle is 0.15–0.20 using the ratio of zero-temperature critical current from spin Hall switching and estimated spin current density for switching the magnet. We show bidirectional transient switching using spin–orbit generated spin torque at 100 ns switching pulses reliably followed by transient read operations. We finally compare the static and dynamic response of the SOT-MTJ with transient spin circuit modeling showing the performance of scaled SOT-MTJs to enable nanosecond class non-volatile MTJs.

Index Terms—**High-speed memory, magnetic tunnel junctions, MRAM scaling, spin Hall effect, spin-orbit torque.**

I. Introduction

CONTINUED scaling of electronic devices has enabled unprecedented growth of computing performance in the past few decades. However, as the electronic device technology node approaches 14 nm dimensions [1], further scaling of complementary metal oxide semiconductor (CMOS) field-effect transistors requires the realization of several complex materials and device changes [2]. One of the methods for enabling further scaling in computing performance is by integration of spintronic devices for on-chip embedded memory [3] or spintronic logic [4]. An efficient method of switching magnetic bits is a pre-requisite to enable such integration [4]. In this context, spin transfer torque (STT) switching of nanomagnets driven by CMOS transistors [5] has attracted significant effort. However, traditional STT devices are reliant on high spin polarization in magnetic tunnel junctions (MTJs) due to orbital symmetry dependent spin filtering in oxides (e.g., MgO) [6]. MTJ-based MRAM technology has the following fundamental drawbacks for compatibility with future scaled CMOS technologies: a) incompatibility of the high operating voltages and currents required for MTJ tunnel currents with scaled CMOS; b) large access transistor size required to meet the drive current requirement that limits circuit density; and c) reliability issues created by the high voltage (>0.8 V) and high current (>100 μA) damaging MTJ oxide. Hence, it is of great interest to pursue MTJ switching methods alternative to STT, which would provide high spin polarization at low voltage and low current operation.

Manuscript received December 3, 2016; revised February 14, 2017; accepted May 15, 2017. Date of publication May 23, 2017; date of current version August 17, 2017. Corresponding author: S. A. Bhave (e-mail: bhave@purdue.edu).

Color versions of one or more of the figures in this paper are available online at http://ieeexplore.ieee.org.

Digital Object Identifier 10.1109/TMAG.2017.2707402

The discovery of giant spin–orbit torques (GSOT), giant spin Hall effect (GSHE), and Rashba Effect (RE) [7]–[10], in which large spin-polarized currents are generated transverse to the charge current direction in high-Z metals (such as β-Ta [9], β-W [10], Pt [11]–[13], and doped Cu [14], [15]), may provide a solution to the voltage, current scaling, and reliability problems of magnetic embedded memory. In particular, scaled spin–orbit torque (SOT)-MTJs can have: a) better drivability in scaled CMOS; b) fast switching time approaching 500 ps; c) decoupled read and write paths; and d) improved tradeoff of non-volatility versus write time [16]. Though two access transistors are needed for read/write operations of a three-terminal SOT-MTJ compared to one for a two-terminal MTJ the size of the access transistors for three-terminal device is smaller as the current and the load resistance of SOT-MTJ is much smaller.

II. Description of the Device

We fabricated a three-terminal device which forms the basic cell for the MRAM which has a SOT-induced write mechanism and MTJ-based read out, as shown in Fig. 1, using fabrication technique shown by Aradhya *et al.* [17]. The device material stack comprising substrate/Ta(6)/$Co_{40}Fe_{40}B_{20}$(1.6)/MgO(1.6)/$Co_{40}Fe_{40}B_{20}$(4)/Ta(3)/Ru(3)/Ti(6)/Pt(40) (thicknesses t are in nanometers) is patterned into the geometry, as shown in Fig. 1(A). The device has a narrow rectangular channel of widths $W_{ch} = 400$, 500, and 600 nm and lengths $L_{ch} = 1600$, 2000, and 2400 nm made up of β-Tantalum (β-Ta) which couples via the SOTs to $Co_{40}Fe_{40}B_{20}$ free layer of the MTJ. The small thickness of the free layer is chosen to reduce the demagnetization field and hence the switching energy of the nanomagnet, but it is thick enough to keep the magnetization in the plane of the device. Isometric view of the spin Hall effect (SHE)-MTJ showing the top electrode and bottom electrode is

0018-9464 © 2017 IEEE. Personal use is permitted, but republication/redistribution requires IEEE permission.
See http://www.ieee.org/publications_standards/publications/rights/index.html for more information.

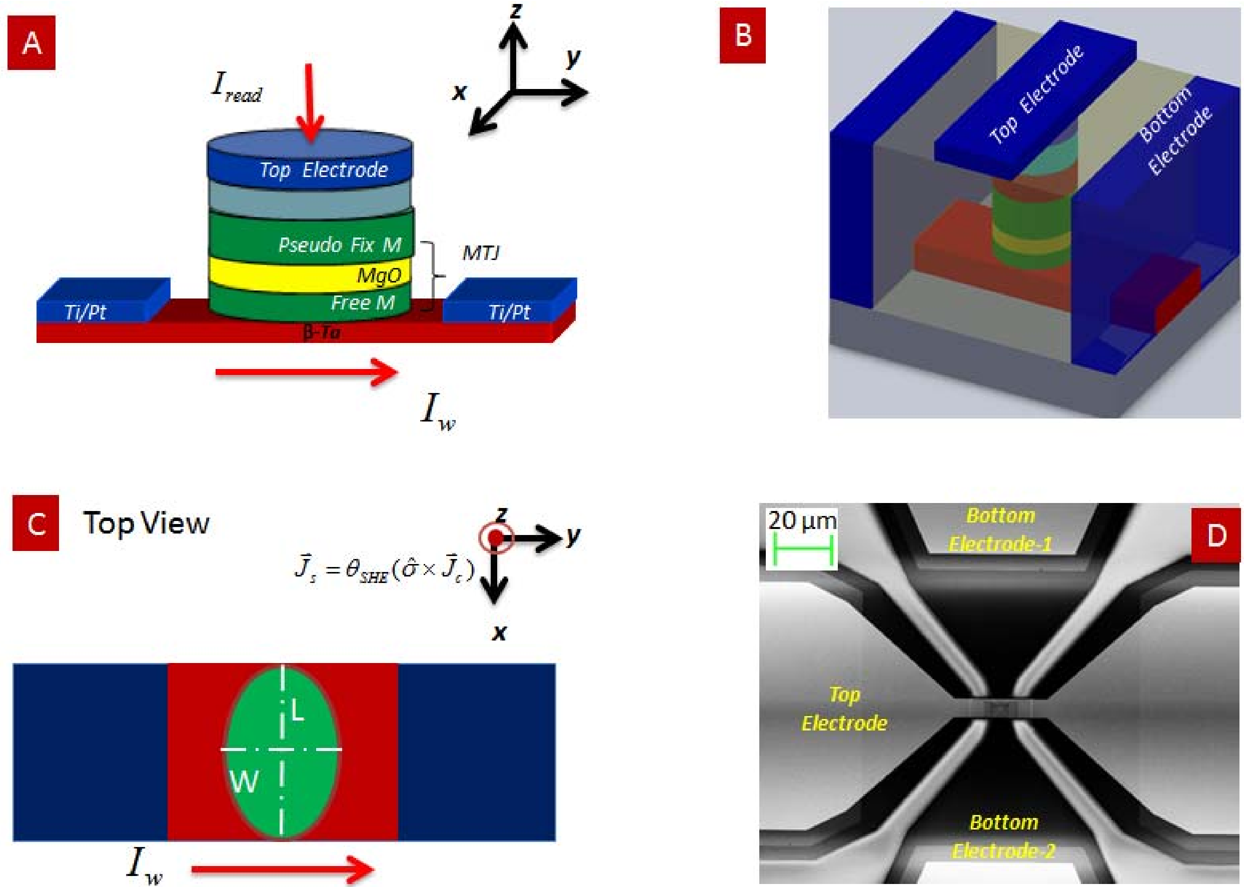

Fig. 1. (A) Three-terminal spin Hall memory device with spin-orbit effect write electrode and MTJ-based readout. (B) Isometric view of the bit showing the device. (C) Top view of the cell showing the orientation of the free layer magnet and the GSOT metal. (D) SEM image of the test structure.

shown in Fig. 1(B). Top view is shown in Fig. 1(C) where the nanomagnet is oriented along the width of the GSOT electrode for appropriate spin injection. Ti/Pt contacts are made to the spin-orbit electrode. This MTJ part of dimension 270 nm × 68 nm was fabricated using E-beam lithography on top of the β-Ta channel.

The top leads of Ti/Pt bilayer were added on the Ta/Ru stack to make contacts to the MTJ. The magnetization state of the cell is written by applying a charge current via the GSOT electrode. The direction of the magnetic writing is set by the direction of the applied charge current. Positive currents (along $+y$ direction) produce a spin injection current with transport direction $(+z)$ and spins polarized in $(+x)$ direction. The injected spin current in its turn produces spin torque to align the nanomagnet in the $(-x)$ direction (since the spin Hall angle for β-Ta is negative). If the direction of the current is switched to the opposite, so is the magnetization direction. The transverse spin current ($\vec{I}_s = \vec{I}_\uparrow - \vec{I}_\downarrow$ with spin direction $\hat{\sigma}$) for a charge current ($\vec{I}_c$) in the write electrode is given by

$$\vec{I}_s = P_{\text{SHE}}(w, t, \lambda_{\text{sf}}, \theta_{\text{SHE}})(\hat{z} \times \vec{I}_c) \tag{1}$$

where P_{SHE}, the spin Hall injection efficiency, is the ratio of magnitude of transverse spin current to lateral charge current, w is the width of the nanomagnet, t is the thickness of the GSHE metal electrode, λ_{sf} is the spin-flip length in the GSHE metal, and θ_{SHE} is the spin Hall angle (coefficient) for the GSHE metal to the FM interface.

We demonstrate bidirectional switching of the three-terminal MTJ using spin injection from the spin-orbit write electrode. The switching diagram of the SHE-MTJ with an external magnetic field is shown in Fig. 2(A). The small signal resistance (dV/dI) is plotted as a function of applied magnetic field, showing a clear hysteresis window with abrupt switching which is representative of a single domain like the behavior of the free layer. The major loop is shown in the inset. The bidirectional current-induced switching is shown in Fig. 2(B) in the presence of an offset field of 102 Oe to center the hysteresis curve for the device. We verify the symmetry of the switching by using a negative offset field (−102 Oe). For positive offset field, the MTJ switches to AP/P when the current through GSOT is positive/negative. When the offset field is reversed, the MTJ switches to P/AP when the current through GSOT is negative/positive. In an integrated device with a synthetic antiferromagnet, the offset field is not necessary and the relationship of the switching and current direction is purely given by (1).

We show the effect of scaling the SOT electrode on the switching of the SOT-MTJ by comparing the dc switching properties for a 270 nm × 68 nm magnet, with SOT electrode of various width: 400, 500, and 600 nm. In Fig. 3(A), bidirectional spin torque switching of the MTJs as a function

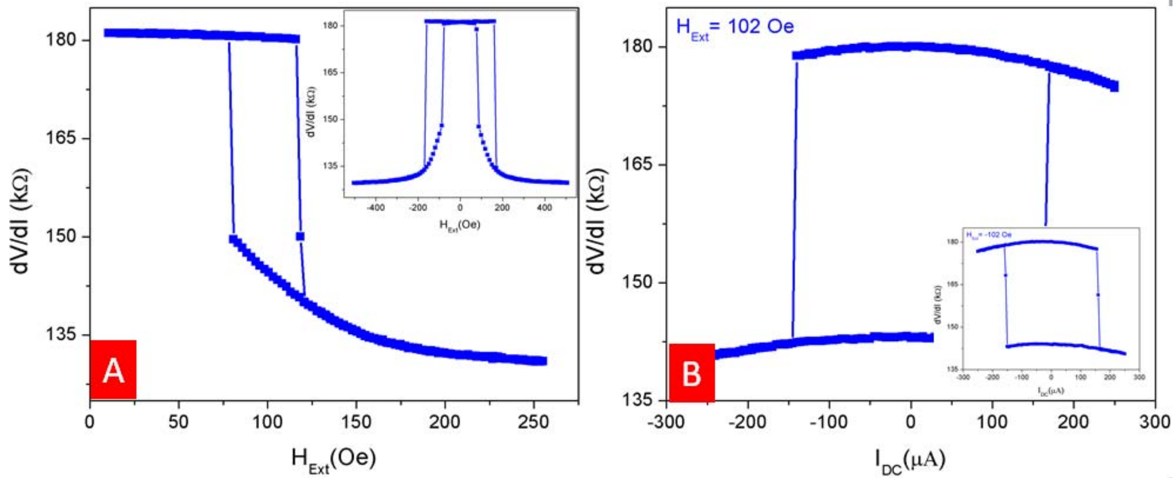

Fig. 2. (A) TMR Minor loop of the MTJ as a function of the external applied in-plane magnetic field H_{Ext} along the long axis of the device. (Inset) TMR major loop of the device. (B) TMR of the MTJ as a function of applied dc current I_{dc}. The measurement was performed with a bias in-plane magnetic field of 102 Oe to center the current loop.

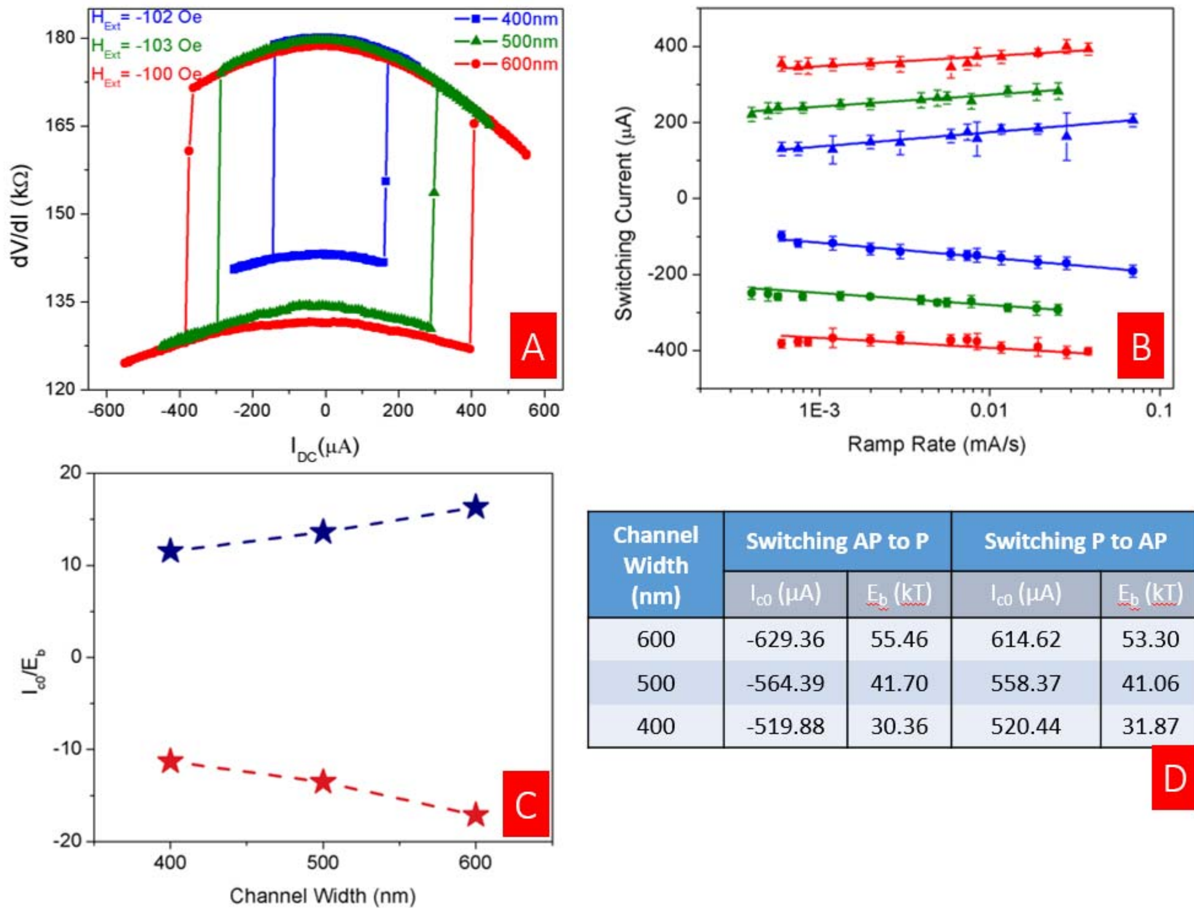

Channel Width (nm)	Switching AP to P		Switching P to AP	
	I_{c0} (μA)	E_b (kT)	I_{c0} (μA)	E_b (kT)
600	-629.36	55.46	614.62	53.30
500	-564.39	41.70	558.37	41.06
400	-519.88	30.36	520.44	31.87

Fig. 3. (A) Effect of channel width reduction on identical magnets switched with spin current injection via SOT. (B) Switching currents as a function of ramp rate for 270 × 68 nm^2 device fabricated on channels of width 600 nm (red line), 500 nm (blue line), and 400 nm (green line). Currents for AP to P switching is shown using circles while P to AP switching is shown using squares. Solid lines represent linear fits of switching current versus ramp rate. Error bars are smaller than the symbol sizes. (C) Linear scaling of critical current normalized by a magnetic barrier with channel width for AP to P and P to AP switching. (D) Table showing values of zero-thermal-fluctuation switching currentI_{c0} and the energy barrier E_b against thermally activated magnetic reversal calculated from linear fits shown in (B).

of applied current in the SOT electrode is plotted. The critical currents for parallel-to-antiparallel switching and vice versa, $I_{\mathrm{cP\text{-}AP}}$ and $I_{\mathrm{cAP\text{-}P}}$, are comparable showing that symmetric bidirectional switching is feasible with SOT switching. Symmetric switching can simplify the constraints on the driving circuitry used for MRAM.

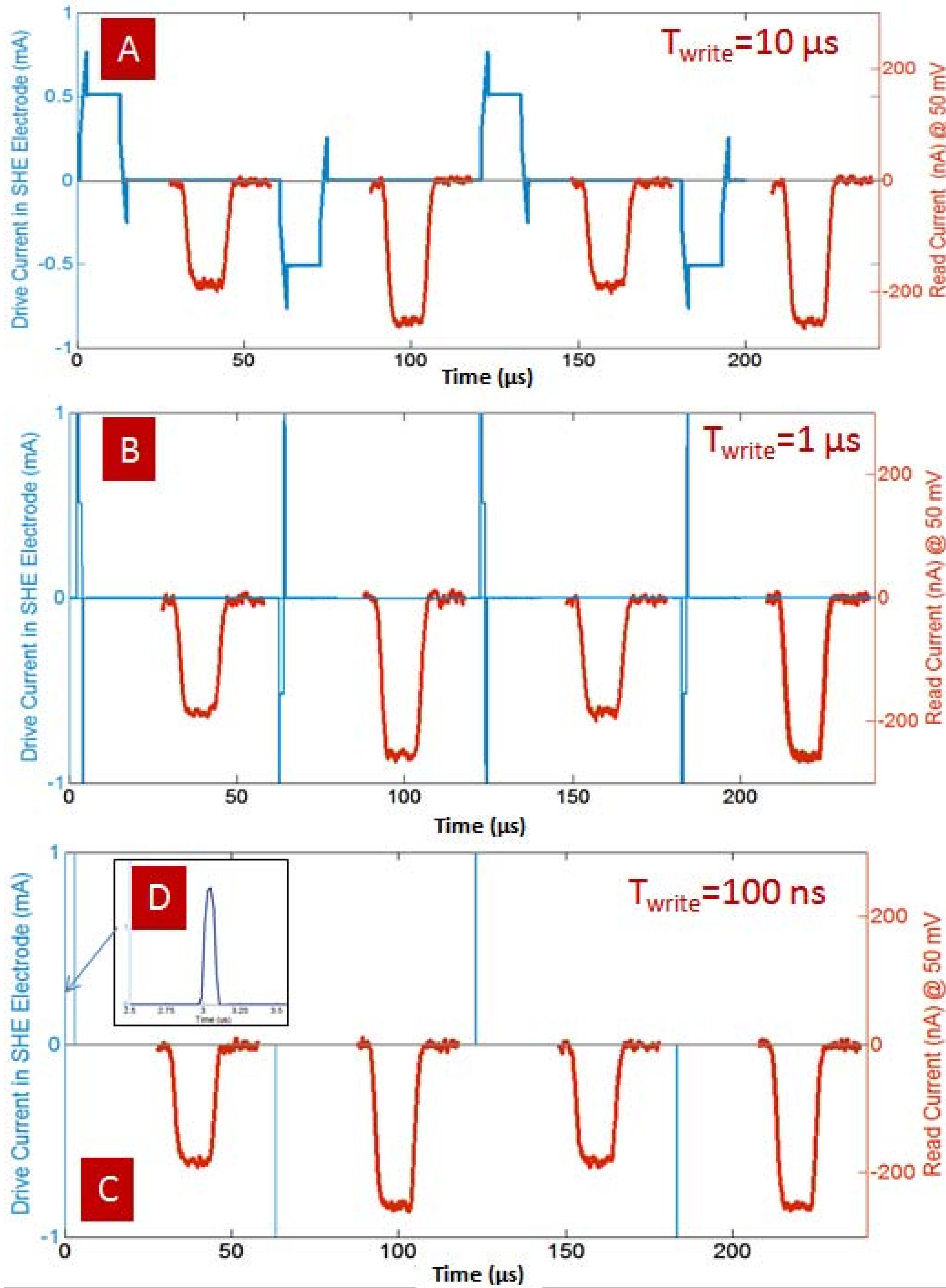

Fig. 4. Transient write and reading of the SHE-MTJ with write pulsewidth. (A) 10 μs. (B) 1 μs. (C) 100 ns. (D) Inset showing the 100 ns width of the write pulse. Read is performed with a 50 mV read voltage pulse applied between the write operations.

We extract the zero-temperature critical currents and magnetic energy barriers for the devices using ramp rate measurements. Fig. 3(B) shows the critical current as a function of ramp rate $\dot{I}_c$. Using thermal activation model, this dependence can be fit to a function form $I_c = I_{c0}$ $[1 - (k_B T/(E_b))\ln((k_B T/(E_b)) \cdot (I_{c0}/\tau_0/(\dot{I}_c)))]$, where the energy barrier E_b and the zero-temperature critical current I_{c0} are the fitting variables, $k_B T$ is the thermal energy [18]. We assume that the temperature of the device was close to room temperature, and the attempt time $\tau_0 \sim$ 1ns. The extracted barriers and zero-temperature critical current are shown in Fig. 3(D). The ratio of the critical current at zero temperature to the energy barrier is plotted in Fig. 3(C) showing linear scaling.

We extract the "effective spin Hall angle" (θ'_{SHE}) for the device by taking the ratio of the expected critical spin current density in STT switching ($J_{s0\text{-MTJ}}$) to the charge current density $J_{c0\text{-SHE}}$ derived from the critical current in spin Hall

switching $I_{c0\text{-SHE}}$ [19]

$$\theta'_{\text{SHE}} = \frac{J_{s0\text{-MTJ}}}{J_{c0\text{-SHE}}} = (W_{\text{ch}} t_{\text{ch}}) \frac{J_{s0\text{-MTJ}}}{I_{c0\text{-SHE}}} = \frac{(W_{\text{ch}} t_{\text{ch}})}{I_{c0\text{-SHE}}} \times \left(\frac{2e}{\hbar} \mu_0 M_s t'_m \alpha \left(H_k + \frac{M_{\text{eff}}}{2} \right) \right). \quad (2)$$

The calculated spin Hall angles for the three devices are 0.16 ($W_{\text{ch}} = 400$ nm), 0.18 ($W_{\text{ch}} = 500$ nm), and 0.20 ($W_{\text{ch}} = 600$ nm). Here the magnet thickness without the dead layer is t'_m, the saturation magnetization is M_s, the effective demagnetization is M_{eff}, the material anisotropy effective field is H_k, and Gilbert damping is α. We assumed a dead layer of 0.2 nm [20]. This technique for extracting effective spin Hall angle is approximate due to the following factors: a) the approximate estimate of the dead layer thickness $(t_m - t'_m)$; b) $I_{c0\text{-SHE}}$ is not exactly proportional to W_{ch} showing a large offset; and c) ignoring the contribution of the field-like torque arising due to reflection of spins at the interface and due to the interface RE.

We also calculate the effective spin injection efficiency in the measured spin-orbit effect device

$$P_{\text{eff}} = \frac{I_{s0\text{-MTJ}}}{I_{c0\text{-SHE}}} = \frac{\pi ab J_{s0\text{-MTJ}}}{4 I_{c0\text{-SHE}}} \approx 96 - 113\% \quad (3)$$

and show that the critical current in SHE is $\sim 2\times$ smaller the critical current in STT with MTJ spin-polarized P_{MTJ} currents

$$\frac{I_{C0\text{-MTJ}}}{I_{c0\text{-SHE}}} = \frac{P_{\text{SHE}}}{P_{\text{MTJ}}} \sim 2. \quad (4)$$

The above effective spin Hall angle is calculated under the assumption that the spin torque is only due to Slonczewski spin torque.

We obtain intrinsic bulk spin Hall angle to be 0.35–0.44 by accounting for the finite interface conductivity, the interface transmission coefficient, and spin diffusion from the second surface of β-Ta, which suppress the spin injection into the magnet. The effect of finite interface reflectivity, i.e., the imaginary component of the mixing conductance ($\tilde{G}^{\uparrow\downarrow}$) and spin diffusion from bottom interface under a semi-classical spin diffusion equation [21] is given by

$$\theta'_{\text{SHE}}(t) = \theta_{\text{SHE}} \frac{(1 - e^{-t/\lambda_{\text{sf}}})^2}{(1 + e^{-2t/\lambda_{\text{sf}}})} \times \left[\frac{|\tilde{G}^{\uparrow\downarrow}|^2 + \text{Re}[\tilde{G}^{\uparrow\downarrow}] \tanh^2(t/\lambda_{\text{sf}})}{|\tilde{G}^{\uparrow\downarrow}|^2 + 2\text{Re}[\tilde{G}^{\uparrow\downarrow}] \tanh^2(t/\lambda_{\text{sf}}) + \tanh^4(t/\lambda_{\text{sf}})} \right] \quad (5)$$

where $\tilde{G}^{\uparrow\downarrow}(t) = G_{\text{mix}} 2 \rho_{\text{Ta}} \lambda_{\text{sf}} \tanh(t/\lambda_{\text{sf}})$ is a scaled spin mixing conductance accounting for thickness (t) induced effect, ρ_{Ta} is the resistivity, and λ_{sf} is the spin-flip length in Ta [20].

III. Transient Switching of the Device and Comparison to Spin Circuit Model

We show the operation of the three-terminal SOT device as a memory element by performing consecutive write and read cycles. The write cycles are performed at $4\times$ the critical current (we note that such high biasing is not possible with tunnel junction-based spin torque switching) followed by a read pulse of amplitude 50 mV applied to the third terminal of the MTJ. The repeatable bidirectional transient switching current and voltage data are plotted in Fig. 4. Fig. 4(A) shows the switching of the device with 10 μs pulsewidth write pulses followed by a read pulse of 10 μs width with $\sim$100 nA of write currents. Fig. 4(B)–(D) shows the read and write operations of the SOT-MTJ with progressively lower pulse widths down to 100 ns. The pulse shape for 100 ns switching is shown in the inset of Fig. 4(D).

IV. Vector Spin Circuit Modeling of Spin–Orbit Torque Switching Devices

We model the SOT-MTJ using vector spin circuit theory [22] comprising 4×4 conduction matrix formulation for spin transport coupled with magnetization dynamics. The circuit model is shown in Fig. 5. The proposed model can be self-consistently coupled to the nanomagnet dynamics including the thermal stochastic noise effects [23]. The spin torque acting on the free layer in an SOT-MTJ originates from: a) spin torque due to spin injection from the fixed layer and b) spin torque due to the SOT acting on the free layer. The phenomenological equation describing the dynamics of nanomagnet with the magnetic moment unit vector (m) is the modified Landau–Lifshitz–Gilbert–Slonczewski equation [24], [25]

$$\frac{\partial m}{\partial t} = -\gamma \mu_0 [m \times \overline{H}_{\text{eff}}] + \alpha \left[m \times \frac{\partial m}{\partial t} \right] + \frac{1}{e N_s} \overline{I}_{s\perp m}(V, G) \quad (6)$$

where γ is the electron gyromagnetic ratio; μ_0 is the free space permeability; $\vec{H}_{\text{eff}}(T)$ is the effective magnetic field due to material, shape, and surface anisotropies, with the thermal noise component [23]; $\vec{I}_{s\perp} = (\hat{m} \times \hat{m} \times \vec{I}_s)$ is the component of vector spin current perpendicular to the magnetization; and N_s is the total number of Bohr magnetons in the magnet. The dynamics of the MTJ are solved self-consistently with the spin transport in the equivalent circuit models.

The equivalent vector spin circuit for SOT-MTJ comprises of the equivalent spin conductances of the fixed ferromagnet (FM_{fix}) and free ferromagnet (FM_{free}) interfaces to form the MTJ [26]. The vector spin equivalent circuit model for an SOT-MTJ is described in Fig. 5(A). The model comprises of three nodes N0, N1, and N2 to describe the MTJ. The magnetization of top fixed layer and bottom free layer are described by $\hat{m}_{\text{fix}}$ and $\hat{m}_{\text{free}}$. The 4-component conductivity of the FM1 and oxide interface is described by G_{FM1} and conductivity of the FM2 and oxide interface is described by G_{FM2}. The conductance matrix describing the spin transport across an FM/Oxide interface can be written as

$$\begin{bmatrix} I_c \\ I_{\text{sx}} \\ I_{\text{sy}} \\ I_{\text{sz}} \end{bmatrix} = \begin{bmatrix} G_{11} & \alpha(V_c) G_{11} & 0 & 0 \\ \alpha(V_c) G_{11} & G_{11} & 0 & 0 \\ 0 & 0 & G_{\text{SL}}(V_c) & G_{\text{FL}}(V_c) \\ 0 & 0 & -G_{\text{FL}}(V_c) & G_{\text{SL}}(V_c) \end{bmatrix} \times \begin{bmatrix} V_c \\ V_{\text{sx}} \\ V_{\text{sy}} \\ V_{\text{sz}} \end{bmatrix} \quad (7)$$

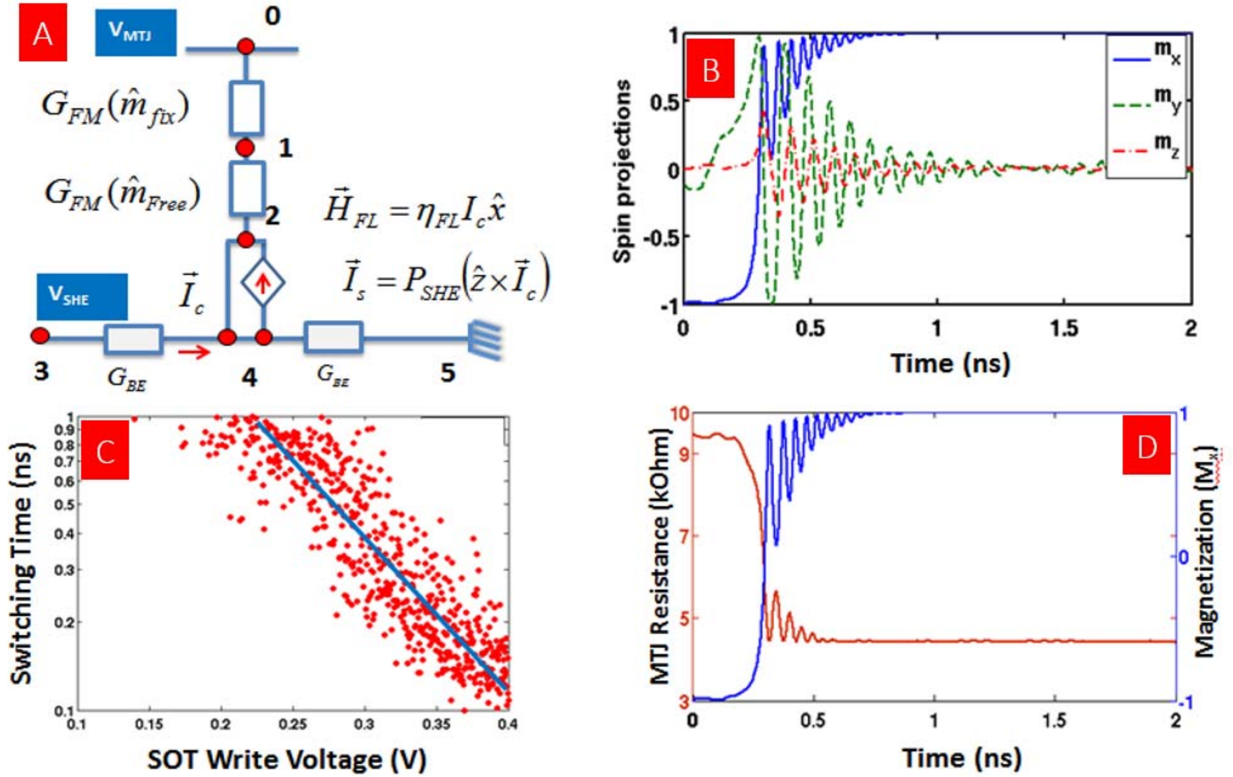

Fig. 5. (A) Transient magnetization switching of the SOT-MTJ nanomagnet. (B) Transient resistance switching of the SOT-MTJ. (C) Stochastic simulation of SOT-MTJ showing nominal switching at 0.4 V applied voltage. (D) Vector spin circuit model of SOT-MTJ with antidamping spin current and field-like torques.

where G_{11} is the interface conductivity (per interface) of the FM/MgO interface, α (V) is the spin polarization across the interface as a function of voltage, and $G_{\mathrm{SL}}(V_c)$ and $G_{\mathrm{FL}}(V_c)$ are Slonczewski and field-like torque contributions from the tunneling spin current across the interface. The voltage dependence of spin polarization α (V), $G_{\mathrm{SL}}(V)$, $G_{\mathrm{FL}}(V)$ is dependent on the detailed band structure of the electrodes and tunneling materials [6], [27], [28]. The effect of magnetization rotation for a precessing MTJ can be described using the proposed model, where the four component conductances evolve as a function of the magnetization of the free magnet

$$G_{\mathrm{FM0}}(\hat{m}) = R(\hat{m})^{-1} G_{\mathrm{FM0}}(\hat{x}) R(\hat{m}) \tag{8}$$

where R is a 4-component transformation to rotate the conductance matrices.

The spin torque from tunneling spin currents acting on the magnet and the effect of spin torque from spin–orbit layer are included via a spin injection into the free layer as governed by the physics of spin injection from SOT layer to FM [20], [21]. The equivalent spin circuit model includes a current control spin current to model the injection of spin current from the SOT electrode to the free layer. We also include the field-like component of the SOT via a current controlled effective magnetic field due to the SOT [29]. A coupled simulation of the spin torque dynamics of an MTJ driven by the spin current response from a vector spin circuit model is shown in Fig. 5(A). The vector magnetization dynamics of the free layer are shown in Fig. 5(B), showing magnetic switching under the combined action of antidamping spin torque and effective field due to spin–orbit effects. The circuit simulation captures the change in the state of the MTJ via a 10 mV relative voltage bias across the device. The change in the MTJ resistance is shown in Fig. 5(B). Vector spin equivalent circuit is shown in Fig. 5(C). Switching time versus applied voltage pulse characteristics are shown in Fig. 5(D). The combined effect of field-like spin torque and antidamping torque significantly enhance the speed of switching showing the nominal switching speed of <200 ps for a 70 kT magnet with dimensions of 20 × 60 nm with a spin–orbit metallic electrode of 60 × 60 nm of resistivity 200 μm · cm. We assumed a bulk spin Hall ratio of 0.2 and effective Rashaba field of 4 × 10^{-6} Oe/(A/cm^2) for the transient vector spin simulations.

V. Conclusion

We have demonstrated transient switching and read out of magnetization in a spin orbital (spin Hall) effect MTJ. Scaled SOT metallic electrodes produce a favorable scaling of spin currents. We estimated a 2× improvement in spin current efficiency compares to tunneling STT mechanism. Using zero-temperature critical current extraction, we derive an effective spin Hall angle of 0.2. Accounting for imperfect interfaces, we deduce the intrinsic spin Hall angle to be 0.33–0.40. Using vector spin circuit modeling, we show that further aggressive scaling of dimensions can lead to nanosecond class spin–orbit effect switching devices with non-volatility.

ACKNOWLEDGMENT

The authors would like to thank M.-H. Nguyen from Cornell University for help with fabricating SOT-MTJ devices and with measurement setups. The authors would also thank Prof. D. C. Ralph and Prof. G. D. Fuchs for discussions about devices and measurements, and Dr. P. Gowtham for his encouragement throughout the project. This work was supported in part by the Semiconductor Research Corporation, in part by the Cornell Center for Material Research through NSF MRSEC program under Grant DMR-1120296, and in part by Cornell NanoScale Facility, a node of the National Nanotechnology Infrastructure Network, through NSF under Grant ECCS-0335765.

REFERENCES

[1] S. Natarajan *et al.*, "A 14 nm logic technology featuring 2nd-generation FinFET, air-gapped interconnects, self-aligned double patterning and a 0.0588 μm^2 SRAM cell size," in *IEDM Tech. Dig.*, Apr. 2014, pp. 3.7.1–3.7.3.

[2] K. J. Kuhn *et al.*, "The ultimate CMOS device and beyond," in *IEDM Tech. Dig.*, Sep. 2012, pp. 171–174.

[3] H.-S. P. Wong and S. Salahuddin, "Memory leads the way to better computing," *Nature Nanotechnol.*, vol. 10, no. 3, pp. 191–194, 2015.

[4] D. E. Nikonov and I. A. Young, "Overview of beyond-CMOS devices and a uniform methodology for their benchmarking," *Proc. IEEE*, vol. 101, no. 12, pp. 2498–2533, Dec. 2013.

[5] A. Brataas, A. D. Kent, and H. Ohno, "Current-induced torques in magnetic materials," *Nat. Mater.*, vol. 11, no. 5, pp. 372–381, 2012.

[6] W. H. Butler, X.-G. Zhang, T. C. Schulthess, and J. M. MacLaren, "Spin-dependent tunneling conductance of Fe|MgO|Fe sandwiches," *Phys. Rev. B, Condens. Matter*, vol. 63, p. 054416, Jan. 2001.

[7] I. Mihai Miron *et al.*, "Current-driven spin torque induced by the Rashba effect in a ferromagnetic metal layer," *Nat. Mater.*, vol. 9, no. 3, pp. 230–234, 2010.

[8] L. Liu, T. Moriyama, D. C. Ralph, and R. A. Buhrman, "Spin-torque ferromagnetic resonance induced by the spin Hall effect," *Phys. Rev. Lett.*, vol. 106, no. 3, p. 036601, 2011.

[9] L. Liu, C.-F. Pai, Y. Li, H. W. Tseng, D. C. Ralph, and R. A. Buhrman, "Spin-torque switching with the giant spin Hall effect of tantalum," *Science*, vol. 336, no. 6081, pp. 555–558, May 2012.

[10] C.-F. Pai, L. Liu, Y. Li, H. W. Tseng, D. C. Ralph, and R. A. Buhrman, "Spin transfer torque devices utilizing the giant spin Hall effect of tungsten," *Appl. Phys. Lett.*, vol. 101, no. 12, p. 122404, 2012.

[11] T. Kimura, Y. Otani, T. Sato, S. Takahashi, and S. Maekawa, "Room-temperature reversible spin Hall effect," *Phys. Rev. Lett.*, vol. 98, no. 15, p. 156601, 2007.

[12] K. Ando *et al.*, "Electric manipulation of spin relaxation using the spin Hall effect," *Phys. Rev. Lett.*, vol. 101, no. 3, p. 036601, 2008.

[13] O. Mosendz, J. E. Pearson, F. Y. Fradin, G. E. W. Bauer, S. D. Bader, and A. Hoffmann, "Quantifying spin Hall angles from spin pumping: Experiments and theory," *Phys. Rev. Lett.*, vol. 104, no. 4, p. 046601, Apr. 2010.

[14] A. Fert and P. M. Levy, "Spin Hall effect induced by resonant scattering on impurities in metals," *Phys. Rev. Lett.*, vol. 106, no. 15, p. 157208, 2011.

[15] Y. Niimi *et al.*, "Giant spin Hall effect induced by skew scattering from bismuth impurities inside thin film CuBi alloys," *Phys. Rev. Lett.*, vol. 109, no. 15, p. 156602, 2012.

[16] S. Manipatruni, D. E. Nikonov, and I. A. Young, "Energy-delay performance of giant spin Hall effect switching for dense magnetic memory," *Appl. Phys. Exp.*, vol. 7, no. 10, p. 103001, 2014.

[17] S. V. Aradhya, G. E. Rowlands, J. Oh, D. C. Ralph, and R. A. Buhrman, "Nanosecond-timescale low energy switching of in-plane magnetic tunnel junctions through dynamic oersted-field-assisted spin Hall effect," *Nano Lett.*, vol. 16, no. 10, pp. 5987–5992, Oct. 2016.

[18] E. B. Myers, F. J. Albert, J. C. Sankey, E. Bonet, R. A. Buhrman, and D. C. Ralph, "Thermally activated magnetic reversal induced by a spin-polarized current," *Phys. Rev. Lett.*, vol. 89, no. 19, p. 196801, 2002.

[19] J. Z. Sun, "Spin-current interaction with a monodomain magnetic body: A model study," *Phys. Rev. B, Condens. Matter*, vol. 62, no. 1, p. 570, 2000.

[20] G. Allen, S. Manipatruni, D. E. Nikonov, M. Doczy, and I. A. Young, "Experimental demonstration of the coexistence of spin Hall and Rashba effects in β-tantalum/ferromagnet bilayers," *Phys. Rev. B, Condens. Matter.*, vol. 91, no. 14, p. 144412, 2015.

[21] P. M. Haney, H.-W. Lee, K.-J. Lee, A. Manchon, and M. D. Stiles, "Current induced torques and interfacial spin-orbit coupling: Semiclassical modeling," *Phys. Rev. B, Condens. Matter*, vol. 87, p. 174411, May 2013.

[22] S. Manipatruni, D. E. Nikonov, and I. A. Young, "Modeling and design of spintronic integrated circuits," *IEEE Trans. Circuits Syst. I, Reg. Papers*, vol. 59, no. 12, pp. 2801–2814, Dec. 2012.

[23] W. F. Brown, Jr., "Thermal fluctuations of a single-domain particle," *Phys. Rev.*, vol. 130, no. 5, pp. 1677–1686, Jun. 1963.

[24] J. C. Slonczewski, "Current-driven excitation of magnetic multilayers," *J. Magn. Magn. Mater.*, vol. 159, nos. 1–2, pp. L1–L7, 1996.

[25] L. Berger, "Emission of spin waves by a magnetic multilayer traversed by a current," *Phys. Rev. B, Condens. Matter*, vol. 54, pp. 9353–9358, Oct. 1996.

[26] S. Manipatruni, D. E. Nikonov, and I. A. Young, "Vector spin modeling for magnetic tunnel junctions with voltage dependent effects," *J. Appl. Phys.*, vol. 115, no. 17, p. 17B754, 2014.

[27] T. Z. Raza, J. I. Cerdá, and H. Raza, "Three-dimensional extended Hückel theory-nonequilibrium Green's function spin polarized transport model for Fe/MgO/Fe heterostructures," *J. Appl. Phys.*, vol. 109, no. 2, p. 023705, 2011.

[28] G. Shine, S. Manipatruni, A. Chaudhry, K. C. Saraswat, D. E. Nikonov, and I. A. Young, "Extended Hückel theory for quantum transport in magnetic tunnel junctions," in *Proc. Int. Conf. Simulation Semiconductor Processes Devices (SISPAD)*, 2014, pp. 301–304.

[29] C. F. Pai, M. H. Nguyen, C. Belvin, L. H. Vilela-Leão, D. C. Ralph, and R. A. Buhrman, "Enhancement of perpendicular magnetic anisotropy and transmission of spin-Hall-effect-induced spin currents by a Hf spacer layer in W/Hf/CoFeB/MgO layer structures," *Appl. Phys. Lett.*, vol. 104, no. 8, p. 082407, 2014.